



# Spatially resolved *in situ* defect spectroscopy during tensile tests using a scanning positron beam

Christoph Hugenschmidt<sup>ID \*</sup>, Matthias Thalmayr, Thomas Gigl

Heinz Maier Leibnitz Zentrum (MLZ), Technical University of Munich, Lichtenbergstraße 1, 85748, Garching, Germany

## ARTICLE INFO

**Keywords:**  
Scanning positron beam  
Tensile test  
Defect spectroscopy  
Positron annihilation

## ABSTRACT

We present a novel technique for analyzing materials *in situ* during tensile tests using a scanning positron microbeam. Doppler broadening spectroscopy (DBS) of the 511 keV annihilation line is used to measure the variation of the local defect concentration with a resolution of 250 μm (FWHM). The evolution of the defect distribution during tensile tests is observed by recording two-dimensional (2D) defect maps as a function of stress and strain with an unprecedentedly short measurement time of 35 s per spectrum. We studied Al alloys (AlMg4.5Mn and Al99.5) at different stages of deformation in order to correlate the spatially resolved formation of lattice defects on an atomic level with the macroscopic material properties obtained by the recorded stress-strain curves. The onset of plastic deformation, i.e. the emergence of stress-induced defects, was clearly observed whereas elastic strain (Hook's region) does not lead to changes in DBS spectra. Finally, observing the maximum local defect density enables prediction of the crack formation that is responsible for the specimen's failure.

## 1. Introduction

In materials science, a profound understanding of the microstructure and lattice defects is essential for comprehending and tailoring macroscopic physical properties such as ductility, yield strength, hardness, and fracture toughness. These properties directly influence the performance and reliability of materials in various engineering applications.

The detection and the characterization of defects in technical alloys during or after mechanical loading are crucial for optimizing material performance. This involves improving not only mechanical strength and durability, but also resistance to fatigue, corrosion, and creep. Since plastic deformation is inherently associated with the generation and movement of dislocations, as well as the formation of vacancies elastically bound to dislocation lines, non-destructive analysis methods play a pivotal role in investigating structural changes at the atomic scale [1, 2]. A deeper understanding of defect formation, dynamics and their interactions ultimately leads to the design of materials with tailored properties, paving the way for innovative solutions in high-performance engineering applications.

Positron annihilation spectroscopy (PAS) has become a well-established technique allowing for in-depth defect analysis without compromising material integrity. In particular, PAS is a powerful tool to study the concentration and distribution of open-volume defects such as dislocations and vacancies. There have been a number of

theoretical and experimental positron studies on defects in aluminum and aluminum alloys in the past. In the late 1960s, Hautajarvi et al. performed positron annihilation lifetime spectroscopy (PALS) on deformed Al single crystals. They attributed the observed increase of the positron lifetime after plastic deformation to positron trapping in dislocations [3]. **This, in fact, was not the complete explanation since a dislocation line itself forms a shallow positron trapping potential with a typical binding energy of  $E_b < 100$  meV [2,4–7].** However, dislocations act as important precursor states for the transition of positrons into deeper traps, such as jogs [5,8] or vacancies bound in the stress field around dislocation lines [9,10]. **The positron binding energy in a vacancy elastically bound to a dislocation line was calculated to be 1.0 eV and 1.3 eV for dislocation with a jog [4].** Wider et al. performed first *in situ* PALS experiments on plastic deformed Al and observed an increase of the mean lifetime, but could not identify different types or concentrations of defects [11]. However, Wider et al. determined the positron binding energy to dislocation lines in polycrystalline Al to  $E_b = 36$  meV [12].

We have carried out various positron beam experiments on different technical Al alloys in order to study defects induced by mechanical load. By using Doppler broadening spectroscopy (DBS) of the positron annihilation line we studied several sets of Al samples after exposure to mechanical load. Tensile tests were performed *ex situ* in a tensile-test

\* Corresponding author.

E-mail address: [christoph.hugenschmidt@frm2.tum.de](mailto:christoph.hugenschmidt@frm2.tum.de) (C. Hugenschmidt).

device, and the specimens were released from mechanical load for the DBS measurements. Through this method, we were able to correlate the defect-sensitive line shape parameter "S" with the absolute stress value responsible for creating lattice defects. Additionally, applying a scanning positron beam enabled us to obtain information on the stress-induced defects in asymmetrically deformed Al samples [13].

In a next step, we developed a tensile test device which is operated at high sample voltage (for positron acceleration) inside the UHV sample chamber of the CDB spectrometer at the high intensity positron beam NEPOMUC in order to enable *in situ* DBS on samples during tensile tests. This upgrade allowed us to collect significantly more data in a shorter amount of time using a single specimen without releasing it from the mechanical load or breaking the vacuum [14].

In the present paper, we present a new technique to finally combine both the application of mechanical stress and defect spectroscopy with high spatial resolution on a single sample. In order to enable *in situ* spatially resolved DBS during tensile tests we pursued a novel approach for 2D positron beam scanning. The capabilities of this new technique are demonstrated by observing the formation of lattice defects at different positions and by recording 2D defect maps during tensile tests on two different Al alloys.

## 2. Method: Detection of Lattice Defects by Doppler Broadening Spectroscopy (DBS)

DBS provides valuable information about open-volume lattice defects as these defects act as attractive potential wells that efficiently trap thermalized positrons. After implantation into matter, positrons typically thermalize within a few ps [15,16] before diffusing through the lattice. Finally, the positron annihilates with an electron predominantly into two 511 keV  $\gamma$  quanta either from a delocalized state in the unperturbed lattice or from a trapped state in an open-volume defect. The momentum of the thermalized positron is usually negligible but the much higher momentum of the annihilating electrons results in an angle deviation from 180° and a Doppler shift of the emitted  $\gamma$  quanta. Annihilation of core electrons with higher momenta than valence electrons results in a larger Doppler shift and hence larger broadening of the 511 keV annihilation photo peak. Consequently, the annihilation of positrons trapped in vacancies leads to a narrowing of the annihilation line since the so-called core annihilation probability is significantly lower compared to the defect-free lattice. The broadening of the 511 keV photo peak is usually quantified by the line-shape parameter S which is defined as the fraction of annihilation events within a fixed small energy window in the center of the Doppler broadened annihilation line. In most DBS experiments the relative change of the S parameter is used to compare samples with various types and concentrations of defects produced after thermal or mechanical load, irradiation or due to imperfect sample synthesis.

In materials science and condensed matter physics, monoenergetic positron beams are applied in order to gain depth dependent information about defects. Moreover, the application of a scanning positron microbeam, i.e. a beam with a sub-millimeter diameter, as available at the CDB spectrometer at NEPOMUC allows for laterally resolved defect studies and 3D-defect imaging. Examples are irradiation induced defects in Mg alloys [17] or in Zr-based alloys [18], the local variation of oxygen vacancy concentration in thin film high-Tc superconductors [19], or variation of defect concentration in plastically deformed Al specimens [13].

## 3. Experimental setup

The Coincidence Doppler Broadening (CDB) spectrometer located at the NEutron induced POrton source MUlich (NEPOMUC) [20] at the research neutron source Heinz Maier-Leibnitz (FRM II) of the Technical University of Munich allows for defect spectroscopy by using a positron microbeam [21]. After entering the instrument the remoderated 20 eV

positron beam [22] of NEPOMUC can be accelerated and focused on a transmission-type remoderator for further brightness enhancement to achieve a lateral resolution below 50  $\mu\text{m}$  (FWHM). Without additional brightness enhancement, the beam diameter at the sample position amounts to 250  $\mu\text{m}$  (FWHM). The sample can be biased up to -30 kV in order to vary the positron implantation depth. Until now, for 3D defect imaging, high-resolution positron beam scanning in two dimensions is realized by x-y-piezo translators mounted directly below the sample in the UHV chamber; the third dimension is given by the variable positron implantation depth. The annihilation  $\gamma$ -quanta are detected by up to eight high-purity germanium (HPGe) detectors which are aligned pairwise face-to-face with the sample positioned in the center for coincidence measurements.

Recently, **we have successfully upgraded the instrument for *in situ* defect spectroscopy during application of mechanical load with a tensile test device**, which replaces the usual sample holder with x-y-piezo translators [14]. However, simultaneous 2D beam scanning and performing tensile tests at high voltage and in UHV conditions was not possible until now. Therefore, we pursued a novel approach for spatially resolved defect spectroscopy by beam scanning during tensile tests. The new beam deflection device is based on a permanent magnet, which can be positioned in two dimensions, below the sample during tensile tests.

The cross-section of the CDB spectrometer with its heart piece — the tensile test device including the movable permanent magnet for beam positioning — is shown in Fig. 1. The guidance and sled exhibit clamps for holding a flat specimen with a length of 50 mm and a width of up to 15 mm in the center of the CDBS sample chamber. When performing tensile tests, the sled is pulled in radial direction away from the chamber center, which causes an elongation of the specimen. The motor allows for a maximum load of about 1500 N, and the applied force is measured with an accuracy of 1 N by a force gauge mounted air-sided between blind flange and counter-thread. The inner central part of the tensile-test device can easily be changed via the bottom port of the sample chamber allowing a simple installation of the specimen outside the spectrometer. A detailed description of the tensile test machine of the CDB spectrometer can be found in [14].

For *in situ* DBS with 2D beam scanning during tensile tests we implemented a new method by accounting for the geometrical constraints of the tensile machine mounted in the CDB spectrometer. The principle is based on a movable cylindrical NdFeB permanent magnet (diameter 12 mm, length 30 mm, 0.7 T at the front side) below the sample plane for deflecting the positron beam from the symmetry axis of the sample chamber. The magnet is mounted via an insulator on an aluminum bar which is attached to the center of the blind flange at the bottom port of the sample chamber. A below allows the flange and hence the magnet to be moved by an air-sided x-y-translator, which is powered by two stepper motors. The magnet can be positioned in an area defined by  $0 \leq x \leq 8 \text{ mm}$  and  $3.5 \leq y \leq 16 \text{ mm}$ . In order to allow both, the precise vertical adjustment of the magnet and simple sample change, the inner setup mounted on the blind flange can be moved in perpendicular direction by a z-translator.

The magnetic beam deflector was characterized with a phosphor screen (20 mm diameter) placed at the sample position and imaging with a CCD camera from outside through an UHV window (the angle of view is 45°). For all experiments presented here we used the remoderated positron beam with an intensity in the order of  $5 \cdot 10^7 \frac{\text{e}^+}{\text{s}}$  positrons per second [23,24] and a kinetic energy of 21 keV at the sample position. Fig. 2 shows the beam spots of the 21 keV positron beam on the phosphor screen at the sample position recorded for the magnet at a distance of 3 mm below the screen. The spots were recorded at steps of 2 mm of the stepper motors within a scan area of  $8 \times 10 \text{ mm}$ . The raw image is corrected by  $\sqrt{2}$  resulting from the angle of view of the camera of 45°. As expected from adiabatic magnetic guiding positrons roughly follow the magnetic field lines. It can be seen, that the grid of beam spots exhibits a near equidistant mesh of spots in

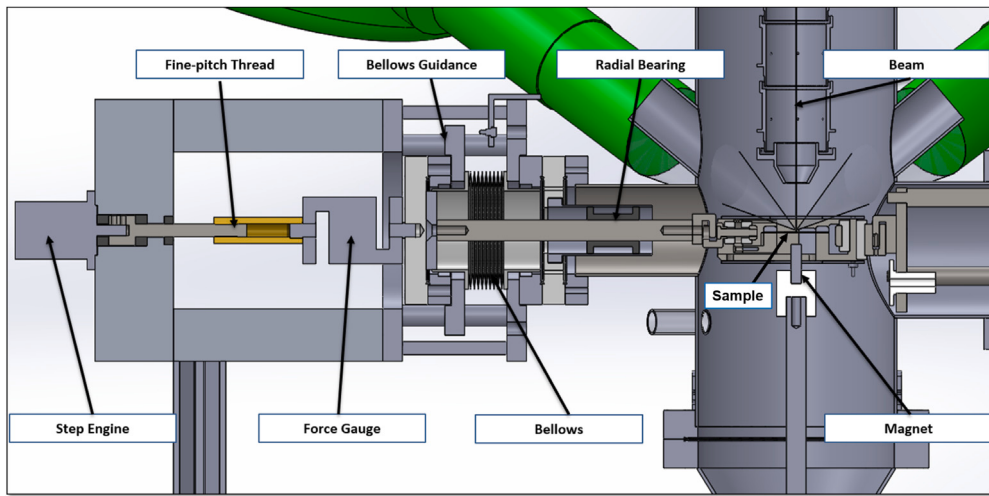


**Fig. 1.** Cross-section of the tensile-test machine at the Coincidence Doppler Broadening (CDB) spectrometer at NEPOMUC: The monoenergetic positron beam is focused onto the sample by electrostatic lenses. The annihilation  $\gamma$ -quanta are detected by up to eight HPGe detectors (green). In the center of the sample chamber, the specimen is clamped in a sled, which is mounted inside a sled guidance and insulated via PEEK insulators. The sled and all moving components are pulled/pushed by a stepper-motor powered bolt which screws in/out a counter-thread. The load is measured by a force gauge mounted air-sided at the blind flange. Below the sample, a cylindrical permanent-magnet is installed on an insulator (white) on top of a bar, which is mounted on a blind flange connected to the sample chamber via bellows at the bottom (not shown). A stepper motor powered x-y-translator is used to move the blind flange and thus the magnet below the sample in two dimensions in order to deflect the positron beam towards the axis of the displaced magnet. An additional z-translator allows the proper adjustment of the magnet-sample distance.

Source: Figure adapted from [14]



**Fig. 2.** Grid of beam spots for a positron energy of 21 keV recorded with a phosphorous screen at the sample position via a camera from outside. The resulting image shows a mesh of equidistant points with 1.66 mm spacing in both directions.

both directions and only very small distortion of the image within the scan area. The quantitative analysis of the recorded beam spots results in their separation on the screen of 1.66(5) mm, i.e. the units of the stepper motors have to be corrected by factor of 0.83(2) to obtain true mm-values of the deflected beam at the sample position.

### 3.1. Sample preparation and measurement parameters

In the present work we studied AlMg4.5Mn and technical Al with a purity of 99.5%. The geometry of the specimens is adapted to the one conventionally applied for uniaxial tensile tests and displayed in Fig. 3. The samples are shaped by milling with a total length of 50 mm, including the broader ends for gripping, whereas the reduced section, i.e. the gauge length, is 2 mm wide and 6 mm long. The thickness of the specimens used here amounts to 1.5 mm and the surfaces are polished in order to unambiguously detect the defects in the bulk created during mechanical load by positron annihilation. Prior to tensile testing, all samples were annealed at 773 K for one hour in argon. The used heat rate was set to 200 K/h and the characteristic time constant of the subsequent cooling was  $\tau=86$  min.

We performed *in situ* DBS during tensile tests at the CDB spectrometer at NEPOMUC by using the positron microbeam with a diameter of 250  $\mu\text{m}$  (FWHM) at the sample position. All measurements are performed with a positron energy of 21 keV corresponding to a mean positron implantation depth in Al of 1.9  $\mu\text{m}$ . For each stage of the performed tensile test the stress applied and the elongation of the specimen are measured. All displayed stress ( $\sigma$ ) and strain ( $\epsilon$ ) values are given for engineering stress and strain, respectively, i.e.  $\sigma$  and  $\epsilon$  are derived from the applied force and elongation with respect to the initial cross section of the sample. The calculated  $S$  parameters of the Doppler broadened 511 keV photo peak result from first evaluating the spectra of each detector and averaging the obtained  $S$  values over all four detectors. The measurement time for the  $\gamma$  spectra was set to 35 s. This leads to an unprecedented short recording time of 2D  $S$  parameter maps of, e.g. less than 50 min for an area of  $4 \times 4 \text{ mm}^2$  with a resolution of 250  $\mu\text{m}$  and a step width of 500  $\mu\text{m}$ .

## 4. Measurements and results

We carried out spatially resolved *in situ* DBS measurements during mechanical load on the alloy AlMg4.5Mn and technical Al99.5 in order to demonstrate the capabilities of the new technique. First, we perform *in situ* tensile tests of an AlMg4.5Mn sample and determine the  $S$  parameter for each stage of the  $\sigma$ - $\epsilon$  curve at five selected spots within the reduced section, i.e. in the 6 mm gauge length, of the sample (see Fig. 3). In Fig. 4 the correlation of mechanical stress  $\sigma$  and the  $S$  parameter measured at five different positions is displayed for the annealed AlMg4.5Mn specimen. In the stress-strain curve the initial elastic region can be distinguished clearly (see also Fig. 5). The measured ultimate strength of  $R_m = 274 \text{ N/mm}^2$  reached at a strain of  $\epsilon \approx 10\%$  is very well within the range given for AlMg4.5Mn ( $R_m = 270\text{--}275 \text{ N/mm}^2$ ). The observed elongation at fracture  $A = 13.3\%$  is also consistent with theoretical values  $A \geq 12\%$ . All curves of the  $S$  parameter, measured at the different spots, show a similar behavior that also goes conform with the course of the stress-strain curve. For strains after the ultimate tensile strength is reached, i.e. for  $\epsilon > R_m$ ,  $S$  increases for spots (2) and (3) but remains rather constant for spots (1), (4) and (5). This behavior is explained by necking of the sample which restricts the further deformation of the specimen to the corresponding area of

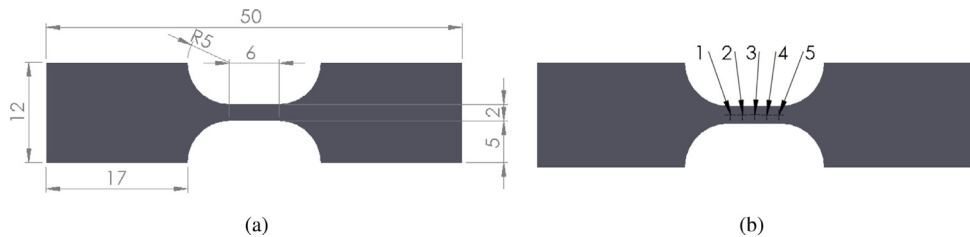


**Fig. 3.** (a) Sample geometry for tensile tests (values in mm). The thickness of the Al samples amounts to 1.5 mm. (b) Definition of five different measurement spots on the sample for the measurement shown in [Fig. 4](#).

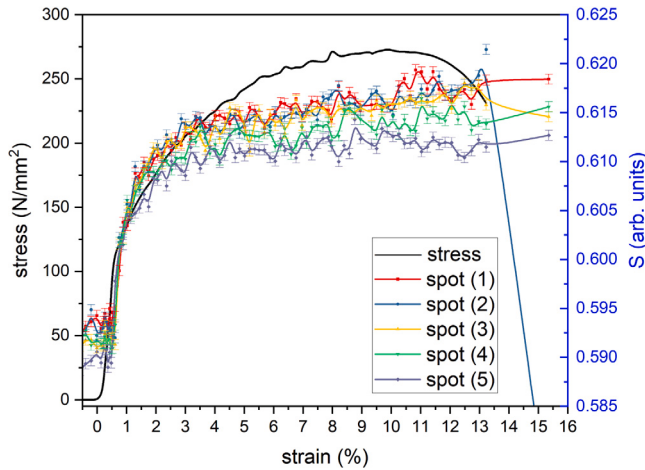


**Fig. 4.** Correlation of mechanical stress and  $S$  parameter in annealed AlMg4.5Mn: The stress-strain curve (black) steeply increases (Hook region) followed by the plastic deformation with a maximum at  $R_m = 274 \text{ N/mm}^2$  (ultimate strength) and ends at the fracture elongation at 13.3%. The  $S$  parameter is measured at five selected spots within the reduced section of the specimen (see [Fig. 3 b](#)).

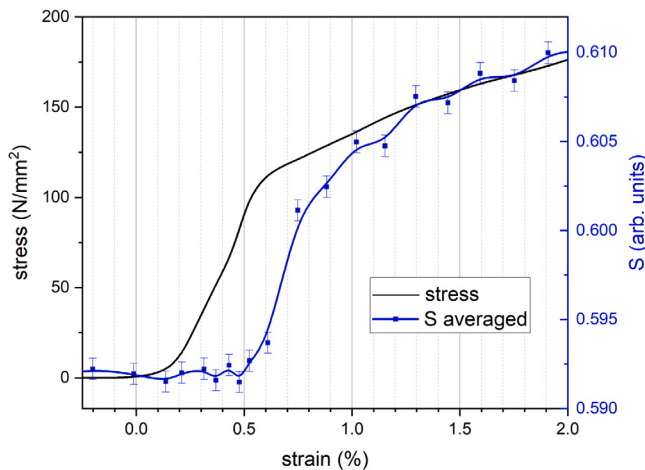


**Fig. 5.** Elastic region and transition to plastic deformation in annealed AlMg4.5Mn: The  $S$  value is averaged over all five spots on the sample. The transition from elastic to plastic deformation is marked by the end of the linear part of the tensile curve and agrees well with the onset of a significant rise of the  $S$  parameter.

spots (2) and (3). In particular, the fracture happens to be exactly at spot (2) which is indicated by a final increase of the  $S$  parameter before break and a distinct drop after the specimen is fractured. The overall increase of  $S$  at the site of fracture amounts to 5.2%. (After failure, the  $S$  signal of the magnet is measured since the beam does not hit the specimen anymore.)

In [Fig. 5](#) a zoom of the initial elastic region and the transition to plastic deformation is displayed for AlMg4.5Mn. The shown curve for  $S$  results from averaging the  $S$  values of all five spots on the sample. As already observed in earlier studies on Al alloys [14], the  $S$  parameter is not sensitive to elastic deformation. The transition from elastic to plastic deformation is marked by the end of the linear section of the tensile curve and perfectly agrees with the onset of a steep increase of the  $S$  parameter. The observed rise is explained by the formation of dislocations and accompanied production of vacancies, causing an enhanced positron trapping rate.

In a next step, we scanned the reduced section of an annealed AlMg4.5Mn specimen with high spatial resolution at selected tensile test stages. A mesh of measurement spots on the sample with a grating constant of 0.5 mm is used. The measurement time per point is set to 35 s. It should be noted that we recorded all scans and the displayed tensile curve with an identical sample. The two-dimensional  $S$  parameter maps recorded by 2D scans at different stages during the tensile test are shown in [Fig. 6](#). The corresponding ten stages of the tensile test are marked in the stress-strain curve shown in [Fig. 6](#) as well. The whole reduced section is scanned as well as a small part of the transition zone between reduced section and the shoulders of the specimen. The noticeable curvature of the contours of the sample in region (5; 9) is not an actual curvature of the sample contours, but presumably a small image distortion. The blurring at the edges of the sample is due to the finite size of the positron beam. The same color code is used for all displayed color maps of the  $S$  parameter.

Before applying stress, a map of the unloaded sample was recorded first, scan (1). This initial scan serves as a baseline for all subsequent measurements of the Doppler broadening  $S$  parameter. Scan (2) shows the elastically deformed sample which does not differ from the previous scan within the accuracy of the  $S$ -parameter ( $\Delta S \leq 9 \cdot 10^{-4}$ ). This is in agreement with the results presented above, confirming that the  $S$  parameter is not sensitive to elastic elongation within the Hook's region. A uniform  $S$  increase over the whole scan area is observed from scan (2) to (3). This increase is attributed to the onset of dislocation movement and the formation of open-volume defects, such as vacancies. The increase is homogeneously distributed, indicating that plastic deformation has begun throughout the sample and is not localized at this stage. Scan (4) exhibits the formation of a distinct region showing increased defect density. The area of increased  $S$  remains present in scans (5) and (6), accompanied by a further overall rise in the  $S$  parameter. This suggests the progression of plastic deformation with continued accumulation of defects. Additionally, an  $S$  gradient becomes visible, particularly in the top-left corner of the sample. This gradient may be attributed to geometric changes in the specimen, such as the enlarging of the transition zone, possibly due to the development of necking. In scan (7), the site of eventual fracture can be predicted for the first time, identifiable as the region with the highest  $S$  value. This corresponds well with the position in the stress-strain curve where the necking typically starts — near the maximum load — which means that the material has reached its maximum tensile strength. At this point, the damage becomes highly localized and the microstructural integrity of the sample is significantly compromised. The  $S$  parameter continues to increase from scan (7) to (8), indicating intensified damage

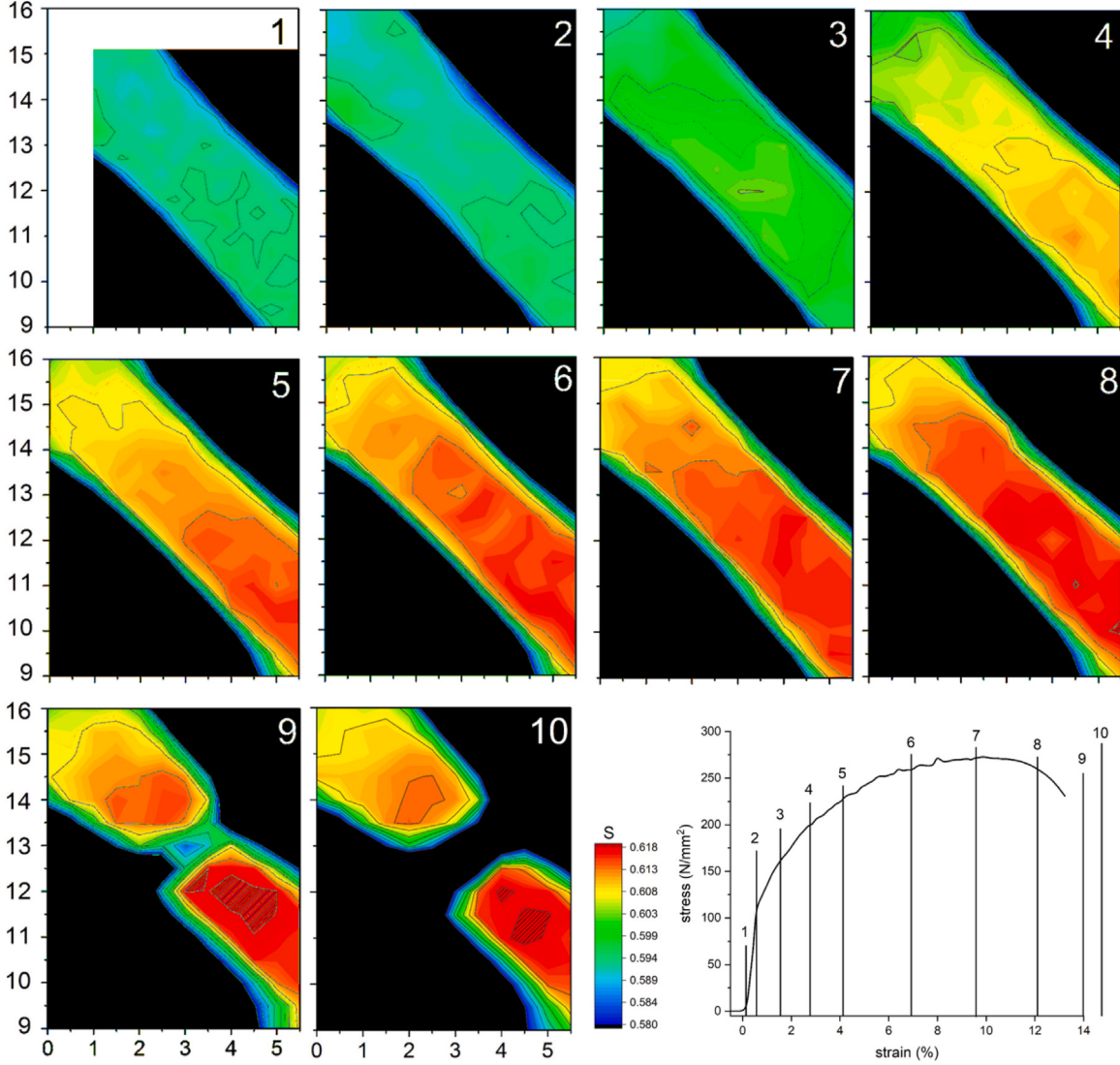


**Fig. 6.** 2D maps of the  $S$  parameter during tensile tests of annealed AlMg4.5Mn at different stages. The shown coordinates correspond to the position units of the magnet used for beam deflection (1 unit  $\hat{=} 0.83$  mm) and the step width of the measurement is 0.5 mm. The stages of the tensile test, set for recording the individual scans, are shown too. The obtained uncertainty of  $S$  is  $\Delta S \leq 9 \cdot 10^{-4}$ . Scan (1) is made at  $\sigma = 0$  while scan (2) is recorded for the sample deformed in the elastic region. Scans (3) to (8) show the sample at different grades of plastic deformation whereas necking starts at (7). Scans (9) and (10) are made of the fractured sample.

accumulation and defect clustering as the material approaches failure. Finally, between scans (8) and (9), the specimen fractures. The fracture occurs in the region with the highest previous defect concentration, which is consistent with the spatially resolved DBS data. Note, that the largest defect concentration, i.e. the maximum density of dislocations and elastically bound vacancies, is observed immediately at fracture in scan (9). The slight overall decrease of  $S$  in scan (10) might indicate a little lower total amount of defects when the stress on the specimen is relieved.

Analogous to the previous measurement, we scanned an annealed Al99.5 specimen with high spatial resolution at selected tensile test stages. For the 2D  $S$  parameter scan, the same grating constant of 0.5 mm and measurement time per point of 35 s are chosen. The locally resolved  $S$  parameter maps recorded by 2D scans at twelve stages of the tensile test are shown in Fig. 7. The elongation of the sample between two subsequent scans amounts to 375  $\mu\text{m}$ . We scan a great part of the reduced section of the specimen as well as a part of one transition zone between reduced section and shoulder. As in the previous experiment, the noticeable curvature of the contours of the sample in region (5.5; 8.5) is attributed to a small image distortion in this region. The same

color code for the  $S$  parameter (uncertainty of  $S$  is  $\Delta S \leq 9 \cdot 10^{-4}$ ) is applied for all presented scans of Al99.5.

Scan (1) shows the unloaded specimen for  $\sigma = 0$ . It can be seen that the reduced section exhibits a slightly increased  $S$  parameter when compared to the adjacent transition zone even before loading. This difference may stem from minor pre-existing defects introduced during the gripping and mounting process, possibly due to slight plastic deformation at the clamping interface. The specimen deformed in the elastic region, as shown in scan (2), does not differ significantly from the unloaded reference. This observation is consistent with the notion that the  $S$  parameter is not sensitive to reversible, elastic deformation governed by Hook's law. The onset of plastic deformation is first detected in scan (3), marked by a noticeable increase in the  $S$  parameter within the reduced section. This rise reflects the initiation of irreversible structural changes — such as dislocation generation and movement — that introduce open-volume defects into the crystal lattice. In scan (4), a distinct area of elevated  $S$  emerges, indicating localized accumulation of defects. The area of increased  $S$  remains visible and becomes more pronounced in scans (5) through (7), accompanied by an overall rise in the  $S$  parameter across the reduced section. Additionally, a gradient in the  $S$  parameter becomes apparent near the top-left corner which

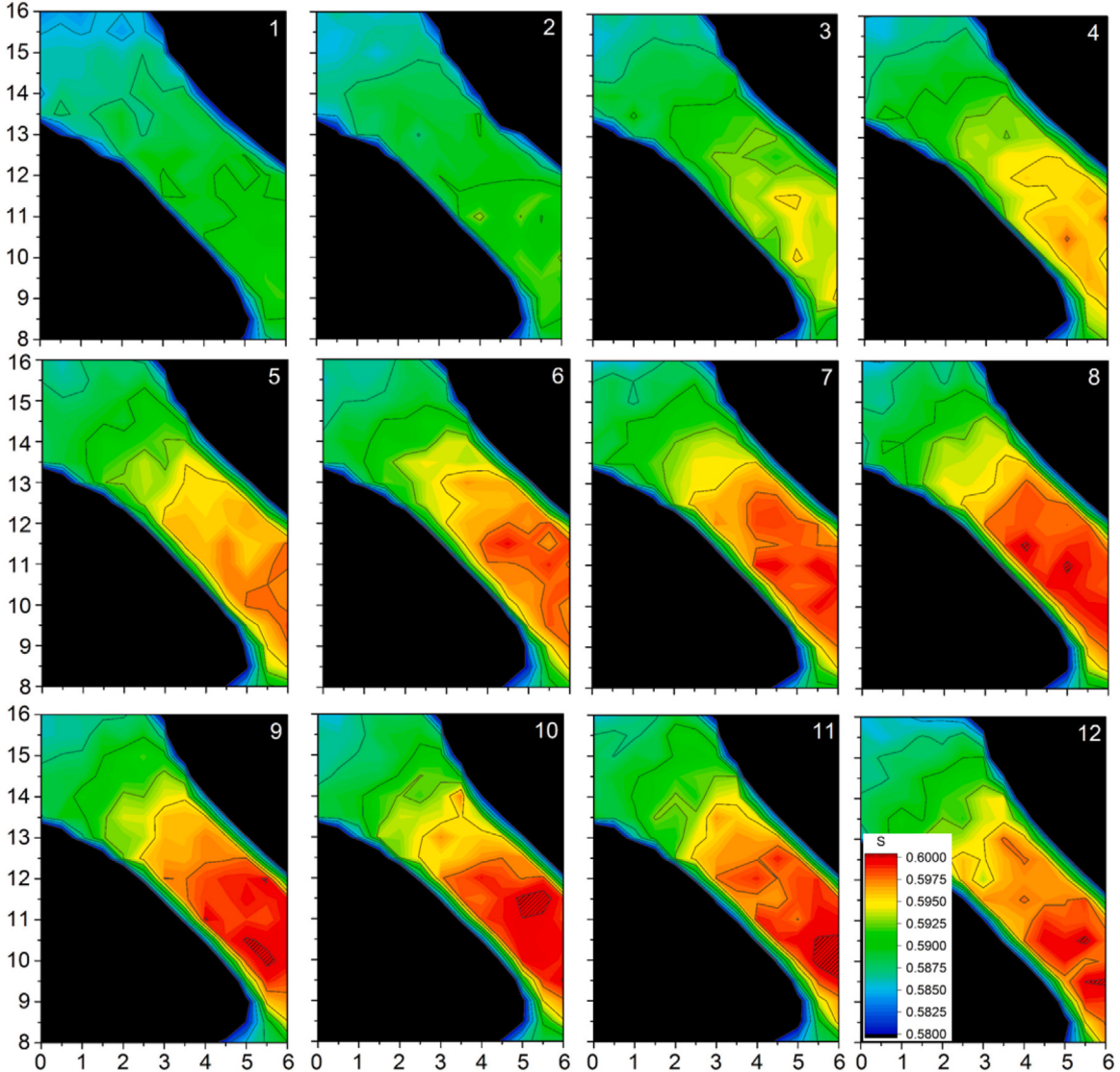


**Fig. 7.** 2D maps of the S parameter during tensile tests of annealed Al99.5 at different stages. The elongation of the sample between two subsequent scans amounts to 375  $\mu\text{m}$ . The shown coordinates correspond to the position units of the magnet used for beam deflection (1 unit  $\hat{=}$  0.83 mm) and the step width of the measurement is 0.5 mm. The obtained uncertainty for S is  $\Delta S \leq 9 \cdot 10^{-4}$ . Scan (1) is made at  $\sigma = 0$  while scan (2) is made of the sample deformed in the elastic region. Scans (3) to (12) show the sample at different grades of plastic deformation, whereat necking is supposed to start at scan (9).

increases from scan to scan. This gradient is associated with geometric changes, i.e. broadening of the transition zone. In scan (8), the entire reduced section exhibits uniformly high S values, and a well-defined boundary forms between the reduced section and the transition zone. In scans (9) through (12), a region with the highest S values persists, appearing to approach a saturation level. Within this zone, only minor fluctuations are observed, and these remain within the measurement uncertainty on the order of  $\Delta S \leq 9 \cdot 10^{-4}$ . Scan (12) was recorded after the specimen had been stretched by a total elongation of 4.125 mm, representing the final stage of deformation. Finally, the specimen fractures, but the fracture site is not located in the scanned area (i.e. at coordinates  $x > 6$  and  $y < 8$ ).

## 5. Discussion

Although the S parameter is not sensitive to minor increases in interatomic spacing — such as those occurring during the elastic deformation of ductile materials — a clear correlation between the S parameter and mechanical stress was found during plastic deformation. The relatively small Hook region observed in the stress-strain curves

is attributed to the pre-treatment of the specimens, particularly high-temperature tempering, which enhances their initial ductility. Upon the onset of plastic deformation, a pronounced and consistent increase in the S parameter was observed across all tested ductile materials. This rise in S is strongly associated with the formation of stress-induced lattice defects, specifically dislocations and vacancies elastically bound to dislocation lines. These open-volume defects serve as efficient positron traps, leading to characteristic changes in the Doppler broadening spectra. As deformation progresses, the rising vacancy density results in higher S values.

Tensile tests on annealed aluminum alloys further revealed a material-specific saturation behavior in the S parameter. For instance, in AlMg4.5Mn, the S value reaches a plateau at a strain of approximately 9%, indicating saturation positron trapping due to the high defect density. Following specimen fracture, the S parameter slightly decreases from its maximum value. This post-fracture reduction has also been reported in earlier studies and may be linked to the annihilation or rearrangement of vacancies as a result of dislocation motion during the saturation regime of plastic deformation [13]. The redistribution of lattice defects in the final stages of deformation likely influences the post-fracture positron trapping behavior.

Local mechanical stress plays a crucial role in the formation of lattice defects, as evidenced by two-dimensional (2D) defect mapping. These 2D DBS maps provide spatially resolved insights into the stress-induced formation of defects and validate the sensitivity and reliability of *in situ* DBS measurements during tensile testing, with a spatial resolution of 250 µm. The 2D mapping technique with DBS has demonstrated stability, reproducibility, and rapid acquisition, enabling precise visualization of defect distributions.

## 6. Conclusion

We have developed a novel device to enable spatially resolved defect imaging during tensile tests by Doppler broadening spectroscopy (DBS) using a monoenergetic positron beam with a standard resolution of 250 µm. A dedicated setup, integrating a beam positioning system with an *in situ* tensile testing machine, was successfully designed and implemented at the CDB spectrometer at the positron source NEPOMUC. The beam scanning system, which is based on a positionable permanent magnet, has been shown to reliably ensure uniform measurement conditions and non-distorted imaging. The beam deflection within the scan region was directly proportional to the magnet position.

The effective use of *in situ* DBS was demonstrated on technical aluminum alloys (AlMg4.5Mn and Al99.5), allowing atomic-scale defect formation to be directly correlated with applied stress and strain. The monoenergetic positron beam enabled two-dimensional defect mapping, revealing local stress distributions and regions of strain concentration, such as necking and transition zones. The observed increase in local defect density provides insights into crack initiation and sample failure prediction. This confirmed DBS as a powerful, non-destructive method for visualizing plastic deformation during *in situ* tensile testing.

Beyond the presented examples, this new analysis technique will be extended to various pre-treated samples, different metals, and technical alloys. It holds particular promise for investigating lattice defect formation in asymmetric samples and welded specimens, facilitating *in situ* 2D imaging of defect evolution in these complex structures.

## CRediT authorship contribution statement

**Christoph Hugenschmidt:** Writing – review & editing, Writing – original draft, Visualization, Validation, Supervision, Resources, Project administration, Methodology, Investigation, Funding acquisition, Conceptualization. **Matthias Thalmayr:** Writing – review & editing, Visualization, Validation, Investigation, Formal analysis, Data curation. **Thomas Gigl:** Writing – review & editing, Supervision, Resources, Methodology, Investigation, Data curation.

## Declaration of competing interest

The authors declare the following financial interests/personal relationships which may be considered as potential competing interests: Christoph Hugenschmidt reports financial support was provided by Federal Ministry of Education and Research Berlin Office. If there are other authors, they declare that they have no known competing financial interests or personal relationships that could have appeared to influence the work reported in this paper.

## Acknowledgments

Financial support by the German federal ministry of education and research (BMBF) within the Project No. 05K22W07 is gratefully acknowledged.

## Data availability

Data will be made available on request.

## References

- [1] A. Seeger, The generation of lattice defects by moving dislocations, and its application to the temperature dependence of the flow-stress of F.C.C. crystals, Phil. Mag. 46 (1955) 1194.
- [2] P.B. Hirsch, D.H. Warrington, The flow stress of aluminium and copper at high temperatures, Phil. Mag. 6 (1961) 735.
- [3] P. Hautojärvi, A. Tamminen, P. Jauho, Trapping of positrons by dislocations in aluminum, Phys. Rev. Lett. 24 (9) (1970) 459–461, <http://dx.doi.org/10.1103/PhysRevLett.24.459>.
- [4] H. Häkkinen, S. Mäkinen, M. Manninen, Edge dislocations in fcc metals: Microscopic calculations of core structure and positron states in Al and Cu, Phys. Rev. B 41 (1990) 12441–12453.
- [5] C. Hidalgo, G. González-Doncel, S. Linderoth, J. San Juan, Structure of dislocations in Al and Fe as studied by positron-annihilation spectroscopy, Phys. Rev. B 45 (13) (1992) 7017–7021, <http://dx.doi.org/10.1103/PhysRevB.45.7017>.
- [6] E. Hashimoto, Temperature dependence of positron trapping to dislocations in deformed zinc, J. Phys.: Conf. Ser. 62 (2) (1993) 552–555, <http://dx.doi.org/10.1143/JPSJ.62.552>.
- [7] K. Petersen, I.A. Repin, G. Trumpy, Positron lifetime analysis of dislocations arising from tensile strain, J. Phys.: Condens. Matter. 8 (16) (1996) 2815–2822.
- [8] E. Hashimoto, Y. Iwami, The positron trapping efficiency of dislocations in deformed dilute aluminium alloys, J. Phys.: Condens. Matter. 6 (1994) 1611–1616.
- [9] V. Chernov, On the calculation of elastic interaction of dislocations with point defects, Phys. Stat. Sol. (A) 68 (1981) 379.
- [10] H.H. S. Mäkinen, M. Manninen, Atomic structure and positron states at dislocation loops in Al, Phys. Scr. T33 (1990) 206–209.
- [11] T. Wider, S. Hansen, U. Holzwarth, K. Maier, Sensitivity of positron annihilation to plastic deformation, Phys. Rev. B 57 (9) (1998-03) 5126–5139, <http://dx.doi.org/10.1103/PhysRevB.57.5126>.
- [12] T. Wider, K. Maier, U. Holzwarth, Temperature-dependent positron trapping in copper and aluminum tubes after tensile deformation, Phys. Rev. B 60 (1) (1999) 179–190, <http://dx.doi.org/10.1103/PhysRevB.60.179>.
- [13] C. Hugenschmidt, N. Qi, M. Stadlbauer, K. Schreckenbach, Correlation of mechanical stress and Doppler broadening of the positron annihilation line in Al and Al alloys, Phys. Rev. B 80 (22) (2009) 224203, <http://dx.doi.org/10.1103/PhysRevB.80.224203>.
- [14] C. Hugenschmidt, M. Thalmayr, T. Gigl, In-situ positron annihilation spectroscopy during tensile tests on Al alloys, Appl. Phys. A 130 (3) (2024) 147, <http://dx.doi.org/10.1007/s00339-024-07301-4>.
- [15] P. Schultz, K. Lynn, Interaction of positron beams with surfaces, thin films, and interfaces, Rev. Modern Phys. 60 (3) (1988) 701–779.
- [16] R. Krause-Rehberg, H.S. Leipner, Positron Annihilation in Semiconductors, Springer, Berlin, Heidelberg, New York, 1999.
- [17] M. Stadlbauer, C. Hugenschmidt, K. Schreckenbach, P. Böni, Investigation of the chemical vicinity of crystal defects in ion-irradiated Mg and a Mg-Al-Zn alloy with coincident Doppler broadening spectroscopy, Phys. Rev. B 76 (17) (2007) 174104, <http://dx.doi.org/10.1103/PhysRevB.76.174104>.
- [18] R. Hengstler-Eger, P. Baldo, L. Beck, J. Dorner, K. Ertl, P. Hoffmann, C. Hugenschmidt, M. Kirk, W. Petry, P. Pikart, A. Rempel, Heavy ion irradiation induced dislocation loops in AREVA's MS® alloy, J. Nucl. Mater. 423 (1–3) (2012) 170–182, <http://dx.doi.org/10.1016/j.jnucmat.2012.01.002>, URL <http://www.sciencedirect.com/science/article/pii/S0022311512000062>.
- [19] M. Reiner, T. Gigl, R. Jany, G. Hammerl, C. Hugenschmidt, Detection and imaging of the oxygen deficiency in single crystalline YBa<sub>2</sub>Cu<sub>3</sub>O<sub>7-δ</sub> thin films using a scanning positron beam, Appl. Phys. Lett. 106 (11) (2015) 111910, <http://dx.doi.org/10.1063/1.4916032>, URL <http://scitation.aip.org/content/aip/journal/apl/106/11/10.1063/1.4916032>.
- [20] C. Hugenschmidt, G. Kögel, R. Repper, K. Schreckenbach, P. Sperr, B. Straßer, W. Tritschhäuser, Monoenergetic positron beam at the reactor based positron source at FRM-II, Nucl. Instr. Methods B 192 (1–2) (2002) 97–101, [http://dx.doi.org/10.1016/S0168-583X\(02\)00788-7](http://dx.doi.org/10.1016/S0168-583X(02)00788-7), URL <http://www.sciencedirect.com/science/article/B6TJN-4CND5D-2/5b81667e156795c9da1d21b591f4b683>.
- [21] T. Gigl, L. Beddrich, M. Dickmann, B. Rienäcker, M. Thalmayr, S. Vohburger, C. Hugenschmidt, Defect imaging and detection of precipitates using a new scanning positron microbeam, New J. Phys. 19 (12) (2017) 123007, URL <http://stacks.iop.org/1367-2630/19/i=12/a=123007>.
- [22] C. Piochacz, G. Kögel, W. Egger, C. Hugenschmidt, J. Mayer, K. Schreckenbach, P. Sperr, M. Stadlbauer, G. Dollinger, A positron moderator for the high intensity positron source NEPOMUC, Appl. Surf. Sci. 255 (1) (2008) 98–100, <http://dx.doi.org/10.1016/j.apsusc.2008.05.286>, URL <http://www.sciencedirect.com/science/article/B6THY-4SK07N4-5/2/e912c2a36998a8e4e82ceddd303f3d07>.
- [23] C. Hugenschmidt, H. Ceeh, T. Gigl, F. Lippert, C. Piochacz, P. Pikart, M. Reiner, J. Weber, S. Zimnik, The upgrade of the neutron induced positron source NEPOMUC, J. Phys.: Conf. Ser. 443 (1) (2013) 012079, <http://dx.doi.org/10.1088/1742-6596/443/1/012079>, URL <http://stacks.iop.org/1742-6596/443/i=1/a=012079>.
- [24] C. Hugenschmidt, H. Ceeh, T. Gigl, F. Lippert, C. Piochacz, M. Reiner, K. Schreckenbach, S. Vohburger, J. Weber, S. Zimnik, Positron beam characteristics at NEPOMUC upgrade, J. Phys.: Conf. Ser. 505 (1) (2014) 012029, <http://dx.doi.org/10.1088/1742-6596/505/1/012029>, URL <http://stacks.iop.org/1742-6596/505/i=1/a=012029>.